

# A Feature Movie of SiO Emission 20-100 AU from the Massive Young Stellar Object Orion Source I

L. D. Matthews<sup>1,2</sup>, L. J. Greenhill<sup>1</sup>, C. Goddi<sup>1</sup>, C. J. Chandler<sup>3</sup>, E. M. L. Humphreys<sup>1</sup>, M. W. Kunz<sup>3,4</sup>

## ABSTRACT

We present multi-epoch Very Long Baseline Array (VLBA) imaging of the  $^{28}\text{SiO}$   $v=1$  and  $v=2$ ,  $J=1-0$  maser emission toward the massive young stellar object (YSO) Orion Source I. Both SiO transitions were observed simultaneously with an angular resolution of  $\sim 0.5$  mas ( $\sim 0.2$  AU for  $d=414$  pc) and a spectral resolution of  $\sim 0.2$  km s<sup>-1</sup>. Here we explore the global properties and kinematics of the emission through two 19-epoch animated movies spanning 21 months (2001 March 19 to 2002 December 10). These movies provide the most detailed view to date of the dynamics and temporal evolution of molecular material within  $\sim 20$ -100 AU of a massive ( $\gtrsim 8M_{\odot}$ ) YSO. As in previous studies, we find that the bulk of the SiO masers surrounding Source I lie in an X-shaped locus; the emission in the South and East arms is predominantly blueshifted and emission in the North and West is predominantly redshifted. In addition, bridges of intermediate-velocity emission are observed connecting the red and blue sides of the emission distribution. We have measured proper motions of over 1000 individual maser features and find that these motions are characterized by a combination of radially outward migrations along the four main maser-emitting arms and motions tangent to the intermediate-velocity bridges. We interpret the SiO masers as arising from a wide-angle bipolar wind emanating from a rotating, edge-on disk. The detection of maser features along extended, curved filaments suggests that magnetic fields may play a role in launching and/or shaping the wind. Our observations appear to support a picture in which stars with masses as high as at least  $8M_{\odot}$  form via disk-mediated accretion. However, we cannot yet rule out that the Source I disk may have been formed or altered following a recent close encounter.

---

<sup>1</sup>Harvard-Smithsonian Center for Astrophysics, 60 Garden Street, Cambridge, MA, USA 02138

<sup>2</sup>MIT Haystack Observatory, Off Route 40, Westford, MA USA 01886

<sup>3</sup>National Radio Astronomy Observatory, P.O. Box O, Socorro, NM, USA 87801

<sup>4</sup>University of Illinois at Urbana-Champaign, Department of Physics, 1110 West Green Street, Urbana, IL 61801

*Subject headings:* masers — stars: formation — radio lines: stars

## 1. Introduction

At a distance of  $\sim 414$  pc (Menten et al. 2007; Kim et al. 2008), radio “Source I” in the Kleinmann-Low (KL) nebula of Orion is believed to be the nearest example of a massive young stellar object (YSO). Source I is highly embedded and has no optical or infrared counterpart; at wavelengths of 8 and  $22\mu\text{m}$  Greenhill et al. (2004a) estimated continuum optical depths of  $>300$ . However, high-resolution 7-mm radio continuum observations have revealed an extended ( $\sim 70$  AU across) source that Reid et al. (2007) proposed may be an ionized accretion disk surrounding an early B-type star.

In addition to its proximity, Orion KL has the distinction of being one of only three star-forming regions known to exhibit SiO maser emission (Hasegawa et al. 1986; Zapata et al. 2009), and these masers were definitively linked with Source I by Menten & Reid (1995). SiO masers offer key advantages for studying stellar sources in that they arise at small radii ( $T_{\text{ex}} > 10^3$  K,  $n(\text{H}_2) \sim 10^{10\pm 1}$   $\text{cm}^{-3}$ ), are unaffected by extinction from dust and neutral gas, and can sample gas kinematics via emission line Doppler shifts and proper motions. Moreover, their high brightness temperature makes them observable with extraordinarily high angular resolution using Very Long Baseline Interferometry (VLBI). Indeed, previous VLBI observations have established that the SiO masers lie at projected distances of  $\sim 20$ -100 AU from Source I (Greenhill et al. 1998, 2004b; Doeleman et al. 1999, 2004; Kim et al. 2008). These scales are of considerable interest, since they correspond to regions where accretion is expected to occur and where winds and outflows from YSOs are expected to be launched and collimated. At present, little is known about the dynamics of these regions in higher mass YSOs ( $M_{\star} \gtrsim 8M_{\odot}$ ) owing to the dearth of direct observations with the requisite resolution. Consequently, persistent gaps in our knowledge of the formation process for OB stars have remained (e.g., Bally & Zinnecker 2005; Zinnecker & Yorke 2007; Tan 2008).

We have used the National Radio Astronomy Observatory’s<sup>1</sup> Very Long Baseline Array (VLBA) to monitor the SiO maser emission surrounding Source I at monthly intervals over several years (see also Greenhill et al. 2004b). Our images have higher dynamic range and higher cadence than any observations of the Source I masers to date. Here we showcase our results in the form of 19-epoch movies spanning 21 months. These movies chronicle for the first time the kinematics and evolution of the molecular material  $\sim 20$ -100 AU from a massive

---

<sup>1</sup>The National Radio Astronomy Observatory is a facility of the National Science Foundation operated under cooperative agreement by Associated Universities, Inc.

YSO. This is part of a series of papers examining Source I on 10-1000 AU scales based on VLBA monitoring and complementary observations of other maser and thermal lines using the Very Large Array (VLA) and the Green Bank Telescope (e.g., Goddi et al. 2009a,b and in preparation; Greenhill et al., in preparation; Matthews et al., in preparation). Together, these data are allowing us to forge a comprehensive new picture of Source I and its role in shaping the Orion KL region.

## 2. Observations and Data Reduction

The  $^{28}\text{SiO}$   $v=1$  and  $v=2$ ,  $J=1-0$  transitions toward Source I ( $\alpha_{J2000}=05^{\text{h}}35^{\text{m}}14.5098^{\text{s}}$ ,  $\delta_{J2000}=-05^{\circ}22'30''.4820$ ) were observed using the VLBA between 2001 March 19 and 2002 December 10. The separation between observations was approximately one month, although no usable data were obtained during two months in mid-2002 (Table 1). Observations were made with the 10 antennas of the VLBA, together with a single antenna from the VLA. The  $v=1$  and  $v=2$  transitions were observed simultaneously, each in a single polarization (RR) with a 15.9 MHz bandwidth centered at  $7.5 \text{ km s}^{-1}$  relative to the Local Standard of Rest (LSR). The adopted rest frequencies for the  $v=1$  and  $v=2$  transitions were 43.122024 GHz and 42.820432 GHz, respectively. The data were processed with the VLBA correlator, yielding 512 spectral channels with a spacing of  $\sim 0.2 \text{ km s}^{-1}$  in each of the two IFs. Correlator dump times were 2.097 s. The total integration time on Source I during each epoch (excluding calibration measurements) was  $\sim 6$  hours for each transition.

We performed all data reduction using the Astronomical Imaging Processing System (AIPS). Because our science goals require high precision, high dynamic range measurements, we took particular care to minimize systematic errors in each stage of our reduction and to maintain accurate astrometric registration between the  $v=1$  and  $v=2$  data (which are very sensitive to delay calibration errors because of the 300 MHz frequency separation between transitions). To insure uniform processing of each epoch, we developed a partially automated POPS script to facilitate the implementation of certain reduction steps. These semi-automated steps were interspersed with frequent manual checks of the data.

Corrections for errors in the *a priori* Earth orientation parameter and station positions (computed starting with the USNO 2004b geodetic VLBI solution<sup>2</sup>) were applied to the data, followed by digital sampler corrections for the VLBA correlator. If uncorrected, these position errors will lead to phase and delay errors which subsequently cannot be calibrated out.

---

<sup>2</sup><http://rorf.usno.navy.mil/solutions/2004b/>

Next, a preliminary amplitude calibration was performed using the default gain curves and system temperatures provided by NRAO. Subsequently, an improved amplitude scale and pointing corrections were computed based on comparison of a time series of total-power spectra to a template for each station.

One-time atmospheric delay and instrumental phase and delay offsets between the IFs were estimated from fringe fits to a one-minute portion of a calibrator scan (0528+134 or 4C39.25), followed by a second fringe-fit to both calibrators (including all times) to solve for the residual delays and rates. Solutions for both IFs were derived independently. However, after ensuring that no systematic offsets were present between the two sets of solutions, the rate solutions from IF2 ( $v=1$ ) were copied and applied to IF1 ( $v=2$ ) in order to minimize phase drifts between the two IFs (which may in turn lead to astrometric misalignments between the two frequencies). The time series phase differences for the two IFs for each antenna were examined following these steps to verify that no phase wraps were present during the track.

The amplitude portion of the bandpass calibration was computed using the total power data for the calibrators 0528+134 and 4C39.25, and the phase portion was derived using a complex polynomial fit to the cross-power data of the same calibrators. Time-dependent frequency shifts were then applied to the line data to compensate for changes caused by the Earth’s motion over the course of the observation.

To refine the astrometric position of the maser and further constrain delay-like errors in the calibration that would affect the relative astrometry of the  $v=1$  and  $v=2$  emission, a strong, compact  $v=1$  maser reference feature was identified in each epoch through examination of cross-power spectra on a variety of baselines. Each feature selected (see Table 2) was one that showed roughly constant visibility amplitudes as function of baseline length and orientation. A fringe fit was performed on this reference feature to determine fringe rates. Following this, a fringe-rate analysis was performed to solve for the position of the reference feature relative to the *a priori* correlator position. This analysis was performed outside of AIPS, using a non-linear least-squares algorithm to fit a sinusoid to the measured fringe rates as a function of time and simultaneously solve for a single vertical atmospheric delay error term in the correlator model for each station. The position offsets determined by this method (Table 2) were then applied to both IFs. Typical uncertainties in RA and DEC were 5 mas and 20 mas, respectively. The proximity of Source I to the celestial equator accounts for the larger uncertainty in the latter coordinate.

Self-calibration was performed on the  $v=1$  reference channel, first in phase only, then in both amplitude and phase. Typically a total of  $\sim 25$ -30 iterations was required. Because the source’s position on the sky compromises the  $u$ - $v$  coverage, care was exercised to avoid

artifacts in the clean component models used for each subsequent self-calibration iteration. Final solutions were applied to the full spectral line data sets for both the  $v=1$  and  $v=2$  transitions. Finally, several additional iterations of self-calibration were used to further improve the  $v=2$  solutions before imaging the full line data sets.

Imaging and deconvolution of the fully calibrated SiO data sets were performed using robust weighting (Briggs 1995) with  $\mathcal{R}=0$ . CLEAN boxes were placed around emission regions in each spectral channel individually to reduce the effects of clean biasing (e.g., Cotton 2007). All channels were cleaned to a level of 20 mJy beam<sup>-1</sup>. This depth of cleaning balanced sidelobe removal against the production of deconvolution artifacts that may result from over-cleaning. These data are particularly susceptible to such artifacts as a result of a combination of the source’s location on the sky and the limited  $u$ - $v$  coverage of the array. The resulting deconvolved images have a field-of-view of  $\sim 0''.4$ , and in all cases we used a restoring beam of  $0.55 \times 0.19$  mas with a position angle of  $0^\circ$ . The  $1\sigma$  RMS noise in individual channels ranged from  $\sim 8$ - $10$  mJy beam<sup>-1</sup> for line-free channels (consistent with expected thermal noise) to  $\sim 9$ - $13$  mJy beam<sup>-1</sup> for channels with strong line emission.<sup>3</sup> Our resulting imaging data have higher dynamic range (up to  $\sim 8000$ ) than any previously obtained VLBI maps of the Source I SiO masers and also recover a significantly larger fraction of the total SiO flux (70 – 90%; Matthews et al., in preparation).

Zeroth, first, and second moment maps were computed from each  $v=1$  or  $v=2$  data cube (using the AIPS task MOMNT); combined moments containing both transitions were also produced. Consecutive epochs were registered by maximizing the cross-correlation between maps of the logarithm of the velocity-integrated intensity. This method removes any component of motion caused by a proper motion of Source I (cf. Gómez et al. 2008; Goddi et al., in preparation). When registering maps separated in time by roughly one month, this method appears to be robust to within approximately one pixel (0.05 mas), although for some epochs, misalignments between the two SiO transitions of up to  $\sim 0.3$  mas may be present as a result of residual calibration uncertainties.

---

<sup>3</sup>These are global values based on Gaussian fits to histograms of the pixel values across the entire channel image; the noise may be higher or lower in certain regions of the image depending on the emission distribution.

Table 1. Summary of Observations

Date (1)	MJD (2)	Project Code (3)	Flagged (4)
2001Mar19	51987.5	BG118A	MK
2001Apr16	52015.5	BG118B	MK
2001May18	52047.5	BG118C	...
2001Jun22	52082.5	BG118D	...
2001Jul22	52112.5	BG118E	...
2001Aug24	52145.5	BG118F	SC,HN
2001Sep19	52171.5	BG118G	FD
2001Oct21	52203.5	BG118H	...
2001Nov19	52232.5	BG118I	FD
2001Dec21	52264.5	BG118J	...
2002Jan27	52301.5	BG118K	...
2002Mar02	52335.5	BG118L	MK,Y
2002Apr01	52365.5	BG118M	...
2002Apr29 <sup>†</sup>	52393.5	BG118N	...
2002May27 <sup>†</sup>	52421.5	BG118O	...
2002Jun28	52453.5	BG118P	...
2002Aug09	52495.5	BG129A	BR,Y
2002Sep05	52522.5	BG129B	HN
2002Oct07	52554.5	BG129C	...
2002Nov06	52584.5	BG129D	...
2002Dec10	52618.5	BG129E	...

Note. — Explanation of columns: (1) date of observation; (2) modified Julian date; (3) VLBA project code; (4) stations flagged due to weather or hardware problems: MK (Mauna Kea); SC (St. Croix); HN (Hancock); FD (Fort Davis); Y (VLA); BR (Brewster).

<sup>†</sup>Failed observation

Table 2. Astrometry of  $v=1$  Reference Features

Project Code (1)	Ref. Chan. (2)	$V_{\text{ref}}$ (km s $^{-1}$ ) (3)	$\Delta\text{RA}$ (arcsec) (4)	$\Delta\text{DEC}$ (arcsec) (5)
BG118A	229	+13.4	+0.032	+0.015
BG118B	228	+13.6	−0.015	−0.054
BG118C	338	−10.2	+0.087	−0.077
BG118D*	336	−9.7	+0.098	−0.119
BG118E	336	−9.7	+0.098	−0.119
BG118F	333	−9.1	+0.086	−0.134
BG118G	225	+14.3	+0.022	+0.059
BG118H	334	−9.3	+0.101	−0.078
BG118I	333	−9.1	+0.096	−0.101
BG118J†	334	−9.3	+0.080	−0.094
BG118K	335	−9.5	+0.082	−0.145
BG118L	198	+20.1	−0.050	+0.010
BG118M	338	−10.2	+0.086	−0.055
BG118P	335	−9.5	+0.092	−0.061
BG129A**	335	−9.5	+0.093	−0.084
BG129B	340	−10.6	+0.095	−0.106
BG129C	198	+20.1	+0.033	−0.025
BG129D	338	−10.2	+0.092	−0.084
BG129E	340	−10.6	+0.089	−0.082

Note. — The adopted correlator position was  $\alpha_{J2000}=05^{\text{h}}35^{\text{m}}14.5098^{\text{s}}$ ,  $\delta_{J2000}=-05^{\circ}22'30''.4820$ . Explanation of columns: (1) Observational epoch (see Table 1); (2) IF2 (SiO  $v=1$ ) spectral channel corresponding to the reference feature used for fringe rate analysis and self-calibration; (3) LSR velocity corresponding to the adopted reference channel; (4) & (5) position offsets in right ascension and declination, respectively, in arcseconds, derived for the reference feature through a fringe rate analysis (see § 2).

\*No astrometric solution was possible; values from BG118E were adopted.

†Atmospheric terms were not included in the solution.

\*\*No astrometric solution was possible; the mean of the solutions from BG118P and BG129B was adopted.

### 3. Results

#### 3.1. The SiO Maser Emission Distribution

##### 3.1.1. Total Intensity Images

Total intensity images of the  $^{28}\text{SiO}$   $v=1$  and  $v=2$ ,  $J=1-0$  emission toward Source I are presented in Fig. 1. To guide the reader, several key features of the maser distribution are also illustrated schematically in Fig. 2.

As seen in previous observations of Source I with VLBI resolution (Greenhill et al. 1998; Doeleman et al. 1999; Kim et al. 2008), the bulk of the SiO emission is located within four “arms” of an X-shaped pattern, centered on the position of Source I. Along a position angle of  $\sim 141^\circ$ , a  $\sim 14$ -AU-thick dark band with well-defined inner boundaries is evident, inside of which no SiO maser emission is detected. This zone maintains a constant thickness over many months and harbors the disk-shaped 7-mm continuum source imaged by Reid et al. (2007).

Another key feature of Fig. 1 is the presence of two “bridges” of emission connecting the North and East arms and the South and West arms, respectively. Bridge emission was detected in the  $v=1$  and/or  $v=2$  transitions in all of our observational epochs. The Western bridge was always significantly brighter than the Eastern bridge—the latter typically showing at most a few weak, isolated spots during any given epoch (e.g., Fig. 3). A counterpart to the Western bridge was first seen in the 1997 VLBA images of Doeleman et al. (2004), and those authors noted that it could not be readily explained in the context of existing biconical outflow models for Source I, which assumed that the symmetry axis of the outflow lay along the northwest/southeast direction (cf. Greenhill et al. 1998; Doeleman et al. 1999). Indeed, this bridge emission is now a key piece of evidence demanding a new geometric and dynamical model for Source I (§ 3.2 & 4.1; see also Greenhill et al. 2004b; Kim et al. 2008).

Comparison of the maps of the two SiO transitions in Fig. 1 shows that on average, the  $v=2$  emission arises at smaller projected distances from Source I than the  $v=1$  emission (see also Kim et al. 2008; Goddi et al. 2009a), although there is considerable overlap. To better quantify this, in Fig. 4 we plot histograms of the number of discrete maser features identified in each of the two SiO transitions (see § 3.3) as a function of distance from Source I. To minimize the impact of projection effects, only spots within the four “arm” regions are included. We see that  $v=2$  features dominate at smaller distances from the star, while the  $v=1$  features become more prevalent at larger radii. Beyond  $r \gtrsim 45$  AU,  $v=2$  emission fades, and only  $v=1$  features are observed. The radial offset,  $\Delta r_p$ , between the locations where the peak number densities of  $v=1$  and  $v=2$  features occur is  $\sim 11$  AU. This is substantially



larger than the offsets observed in evolved stars ( $\Delta r_p \lesssim 1$  AU; e.g., Desmurs et al. 2000; Soria-Ruiz et al. 2004; Yi et al. 2005). Furthermore, we find no evidence for variation in the relative distributions of the  $v=1$  and  $v=2$  masers during our monitoring. This too is in contrast to the case of evolved stars, where the relative position of the two transitions may be seen to vary as a function of stellar phase (i.e., on timescales of months; see Gray & Humphreys 2000; Yi et al. 2005). Nonetheless, we cannot yet exclude that changes in the relative distributions of the  $v=1$  and  $v=2$  masers around Source I may evolve on timescales of several years or more.

The presence of an overlap region for the SiO  $v=1$  and  $v=2$  masers provides an interesting constraint on the dominant excitation mechanism for the masers. Purely radiative pumps (e.g., Alcolea 1989; Bujarrabal 1994a,b) do not produce spatial coincidence of the  $v=1$  and  $v=2$  masers. On the other hand, collisional pumps lead to a large amount of overlap in the parameter space for these two transitions (e.g., Lockett & Elitzur 1992), in agreement with our Source I observations.

Preliminary radiative transfer modeling by Goddi et al. (2009a) using a large velocity gradient code provides some insight into the physical conditions (temperature, density) required to produce the observed  $v=1$  and  $v=2$  maser distributions. Using a model that included both collisional and radiative pumping, as well as physical parameters appropriate for the Source I region, Goddi et al. found that the  $^{28}\text{SiO}$   $v=2$  maser will survive in a stronger, hotter radiation field than the  $v=1$  maser and that it will be optimized at higher kinetic temperatures ( $T_k > 2000$  K) where it can become more strongly inverted than the  $v=1$  transition. This is consistent with the observation that  $v=2$  masers tend to arise closer to Source I than the  $v=1$  masers. The Goddi et al. model also predicts overlap in the range of densities where the  $v=1$  and  $v=2$  transitions can occur (i.e.,  $n_{H_2} = 10^8 - 10^{10} \text{ cm}^{-3}$  for  $v=1$  and  $n_{H_2} = 10^9 - 10^{11} \text{ cm}^{-3}$  for  $v=2$ , respectively). This suggests that the mean gas densities within this overlap zone observed around Source I should be  $n_{H_2} \sim 10^{9.5} \text{ cm}^{-3}$ . More sophisticated modelling that treats the effects of maser saturation and line overlap will be presented by Humphreys et al. (in preparation).

### 3.1.2. *The Temporal Evolution of the Intensity Distribution*

A combined map of both SiO transitions, summed over all 19 observing epochs (Fig. 5), reveals the trails of hundreds of individual maser features, underscoring that at VLBI resolutions, Source I is the most complex maser source known. Individual maser features can persist for several months or more, and a significant fraction exhibit detectable motions in the plane of the sky on timescales of a few weeks; see also § 3.3). In addition to the multitude

of maser trails in Fig. 5, elongated, high surface brightness “emission fronts” are visible in three of the arms (see also Fig. 2). These fronts are more prominent in the  $v=1$  transition (cf. Fig. 1). Analogous features have been seen in previous high-resolution images of the Source I SiO masers (Greenhill et al. 1998; Doeleman et al. 1999, 2004), but our new observations show that such structures can remain relatively stable in extent, position, and velocity over many months.

An animated movie (Fig. 5, online version) provides a “4-D” view highlighting the month-to-month changes that give rise to the intricate structures seen in the 19-epoch summed image. While the gross morphology of the maser distribution persists over the length of the movie, significant temporal changes are evident in the positions and brightnesses of thousands of individual features, collectively giving the maser-emitting material an “effervescent” appearance.

Further inspection reveals that the observed motions of the maser features exhibit certain systematic trends. First, outward motions (i.e., away from Source I) are visible along each of the four arms, as well as in several isolated groups of features that are detached from the main arms and bridges (see Fig. 2). Radially outward motions are also observed within the Western bridge region. However, in addition, maser features along the Western bridge clearly display a component of motion *tangential* to the bridge. Interestingly, material along the outer edge of the Western bridge is seen moving to the northwest, while material along the inner edge moves in the opposite sense. These patterns most likely arise from emitting material along the rim of a rotating, geometrically thick disk whose near side is tipped slightly to the southwest (§ 4.1). Motions within the Eastern bridge also appear to be consistent with this picture, although features in this region typically persist for only one or two epochs, making it more difficult to establish systematic trends.

The bright, elongated emission fronts described above pose an interesting contrast to many of the other arm features. Although modest changes in the position angle and small-scale morphology of these fronts are visible from month to month, their general locations and extents remain fairly constant over nearly two years. We also observe gas within these regions whose line-of-sight velocity dispersion ( $\sim 1\text{-}5 \text{ km s}^{-1}$ ) is several times higher than the mean of the surrounding material ( $\sim 0.3 \text{ km s}^{-1}$ ; Fig. 6).

### 3.2. The SiO Radial Velocity Field

In Fig. 7 we show a first moment map obtained from the combined SiO  $v=1$  and  $v=2$  emission on 2001 March 19. Integrated spectra of the two transitions are also shown. The

integrated line profiles of both the  $v=1$  and  $v=2$  emission maintained their characteristic double-peaked shape throughout the course of our monitoring. A more detailed analysis of the spectral line profiles and the temporal variability of the SiO masers will be presented by Matthews et al. (in preparation). Consistent with earlier studies, we also see that the redshifted SiO emission arises primarily from the North and West arms, while the blueshifted emission arises predominantly from South and East arms. Furthermore, our new high dynamic range images showcase some additional characteristics of the SiO distribution that were only hinted at by previous investigations.

Fig. 7 further highlights the two bridges of emission connecting the South and West (blue) arms and the East and North (red) arms, respectively (see also Fig 1 & 5; Greenhill et al. 2004b). We see that emission from both bridges occurs predominantly within a few  $\text{km s}^{-1}$  of the systemic velocity and that a velocity gradient is present in the sense that the material in the northern end of the bridge has (on average) higher radial velocities compared with the material in the southern end. We interpret these observations as signature of rotational motion about an axis oriented along the northeast/southwest direction. In this picture, the red and blue arms represent the receding and approaching sides, respectively, of the rotating structure (see § 4.1).

Another notable feature of Fig. 7 is the presence of clear systematic velocity gradients along each of the four arms—i.e., emission at smaller projected distances from the source tends to have higher radial velocities than emission at larger projected radii. The magnitude of the gradients is  $\sim 0.4 \text{ km s}^{-1} \text{ AU}^{-1}$ . While there had been some indication of velocity gradients along individual arms from earlier imaging studies (Doeleman et al. 2004; Greenhill et al. 2004b), our new data show similar gradients along all four arms, implying that they result from a global rather than a localized phenomenon. This finding has been confirmed independently by Kim et al. (2008) using data from the VERA array. As with the bridge masers, these velocity gradients are difficult to account for in any model of Source I that does not include rotation about a northeast/southwest axis.

An animated version of Fig. 7 (online version) displays the radial velocity fields derived from all 19 epochs of observations. The first moment maps are somewhat noisier than the zeroth moment maps used to produce the animation in Fig. 1, leading to visible north/south artifacts around bright features in some frames. Nonetheless, Fig. 7 helps to highlight the evolution of some of the smallest and faintest detected features, particularly near the bridge regions.

### 3.3. Proper Motions

#### 3.3.1. Methodology

Fig. 8 presents proper motions of individual maser features derived from our data. Here, positions of the maser features during each epoch were measured from two-dimensional Gaussian fits to the SiO total intensity images, while radial velocities were taken to be the intensity-weighted mean velocity at each feature’s location. Our typical detection threshold was  $\sim 10\sigma$ .

The total numbers of maser spots catalogued over 19 epochs were 27,857 in the  $v=1$  line and 15,448 in the  $v=2$  line, respectively. The resulting  $v=1$  and  $v=2$  spot catalogues were then systematically searched to identify features that persisted over at least *three* epochs (Bridge regions) or *four* epochs (all other regions) and appeared to move along linear trajectories in the plane of the sky.

For each of the epochs (beginning with BG118B) an automated search of the preceding epoch was performed for possible counterparts to each of the identified maser spots. The search radius was restricted to 1 mas (corresponding to  $V_{\text{sky}} < 35 \text{ km s}^{-1}$ ), with the additional requirement that the radial velocity change between epochs was less than or equal to  $0.2 \text{ km s}^{-1}$ . The latter criterion corresponds to an acceleration  $< 8 \times 10^{-3} \text{ cm s}^{-2}$ .

For each candidate identified, a line was fit between the position of the initial spot and the candidate to delineate an initial predicted trajectory. The subsequent epoch was then searched for spot candidates lying along the predicted path to within  $\pm 0.15$  mas in  $x$  and  $y$  and  $\pm 0.2 \text{ km s}^{-1}$  in  $V_r$ . The former limit corresponds approximately to our registration uncertainty between epochs, while the latter is comparable to our velocity resolution. Each time a spot was found matching these criteria, a linear least squares fit (in  $x$  and  $y$ ) was performed to the resulting set of three spots to refine the predicted trajectory. Outside of the bridge regions, this procedure was then repeated for the next epoch in the sequence.

Because the region around Source I is so crowded with maser features, there were a number of cases where more than one feature from a given epoch was identified as a candidate for falling on a particular trajectory. For these cases, only the trajectory with the lowest  $\chi^2$  value was used to compute a proper motion vector ( $x_0, y_0, V_{\text{sky}}, \text{PA}$ ) for the final database.

The results of the above analysis are summarized in Fig. 8. Features persisting for more than 3 months (bridge regions) or 4 months (all other regions) are visible as overlapping arrows. Typical feature lifetimes range from less than one month to 3 or 4 months, with occasional features persisting as long as  $\sim 11$  months.

### 3.3.2. Results and Interpretation

A full catalogue and analysis of the SiO maser proper motions will be presented elsewhere (Goddi et al., in preparation), but here we describe a few key trends.

The derived 3-D (space) velocities for individual features range from  $5.3 \text{ km s}^{-1}$  to  $25.3 \text{ km s}^{-1}$ , with a mean of  $14.0 \text{ km s}^{-1}$ . We assume a systemic velocity for Source I  $V_{\text{sys}}=5.5 \text{ km s}^{-1}$ . We find no evidence for any systematic decrease in the magnitudes of the motions in the plane of the sky with increasing distance from the star, suggesting that the radial velocity gradients along the arms (§ 3.2) are not simply the result of a decelerated outflow, but instead arise primarily from differential rotation (see also Kim et al. 2008).

The proper motion vectors plotted in Fig. 8 were derived by conservatively assuming that the motions were linear over 3-4 months and that the radial component of the velocity did not change by more than  $\pm 0.2 \text{ km s}^{-1}$  from month to month. These initial selection criteria may exclude features with significant accelerations. A systematic search for accelerations in the spot motions will be presented in a future paper. However, we note that we already see qualitative evidence of accelerated motions within our data based on the time-integrated distributions of features along the “streamers” and within several “isolated” regions (e.g., the features labeled “A” and “B”, respectively on Fig. 8). Two examples are highlighted in Figs. 9 & 10. Although the motions of *individual* maser clumps within the regions shown in Figs. 9 & 10 cannot be distinguished from linear paths to within positional uncertainties, the time-integrated views reveal the appearance of multiple features over multiple epochs that cluster along curving arcs, as would be expected if the maser-emitting material were being shepherded along twisted magnetic field lines (e.g., Banerjee & Pudritz 2006; see also § 4.3.4).

Other noteworthy features of Fig. 8 include the proper motions along the Western bridge (labeled “C” on Fig. 8), which exhibit a component of radially outward motion in addition to two oppositely directed streams moving tangential to the bridge, as seen in the animated versions of Fig. 5 & Fig. 7. Finally, as indicated by arrow “D”, in the North arm we find that the proper motion vectors twist by  $\sim 90^\circ$  roughly half-way along the arm, again suggestive of material that may be following non-linear paths.

## 4. Discussion

### 4.1. A New Model for the SiO Maser Kinematics

Earlier VLBI observations of SiO masers around Source I established the X-shaped distribution of emission as well as the spatial separation between the red- and blue-shifted arms. Based on these observations, Greenhill et al. (1998) and Doeleman et al. (1999) proposed that the SiO masers arise from limb-brightened edges of a biconical outflow, oriented along a southeast/northwest direction. However, our new, more sensitive observations are better explained by a new model—namely that the masers are associated with an edge-on disk whose rotation axis is oriented along the northeast/southwest direction (see also Greenhill et al. 2004b; Kim et al. 2008). Support for this model comes from the radial velocity gradients along each of the four arms (indicative of differential rotation), as well as the presence of the bridge emission and its associated velocity gradients (§ 3.2). Furthermore, the canting of the maser arms (Fig. 5) suggests a reflexive symmetry about a plane whose position angle ( $PA \approx 141^\circ \pm 1^\circ$ ) closely matches the ridge of 7-mm continuum emission observed by Reid et al. (2007) on 2000 November 10 ( $PA \approx 142^\circ \pm 3^\circ$ ). The presence of the well-defined dark band in Fig. 5 (see § 3.1.1) also suggests that the conditions favorable for excitation of the SiO masers set in rather abruptly at a fixed scale height above a flattened, disk-like structure.

Underlying the new kinematic model for Source I is the assumption that the SiO masers trace real, physical motions of gas clumps rather than, e.g., illumination patterns or shocks transversing a fixed medium. The contrast between the pattern of motions observed in the Western bridge versus the arms (§ 3.3) strongly supports this interpretation, as shocked material would not be expected to have two apparent kinematic components (both tangential and radially outward). Moreover, owing to gradients in temperature and density between regions close to the disk plane and the outer reaches of the wind, shock conditions are unlikely to be similar over the scales of tens of AU from Source I where maser motions are observed. Finally, the multitude of linear maser trails seen in Fig. 5 also supports a kinematic interpretation for the SiO masers; features that move many times their characteristic sizes without significantly changing morphology would not be expected to arise as a shock front transverses a clumpy, inhomogeneous medium and are a strong indicator that we are tracing motions of individual clumps.

### 4.2. The Mass of Source I

One of the longstanding controversies surrounding Source I has been the mass of the central star. While our present data can offer important new constraints on this quantity,

obtaining a precise mass estimate is complicated by the likelihood that the maser-emitting material is not in purely Keplerian rotation (see also Kim et al. 2008). For example, some degree of turbulence is almost certain present in the gas (e.g., as evidenced by small-scale complexities in the radial velocity fields in the arm regions), and the outward motions of the maser clumps (§ 3.3) imply forces acting on the maser gas opposite to those of gravity (e.g., radiative and/or magnetic forces). Such effects can lead to underestimates of the enclosed mass (e.g., Königl & Pudritz 2000; Piétu et al. 2005; Bujarrabal et al. 2005). Moreover, the disk itself might contain up to a few solar masses of material (Reid et al. 2007) and thus have a non-negligible mass relative to the central source.

One means of estimating of the mass of Source I comes from the observed transverse motions of maser features in the Western bridge region (Fig. 8). We assume that the bridge features lie at  $r \sim 35$  AU in a circularly rotating disk (i.e., just outside the edge of ionized inner disk measured by Reid et al. 2007) and that the Source I disk has a nearly edge-on inclination to our line-of-sight ( $i \sim 85^\circ$ ). Taking the mean space motion of the  $v=2$  bridge features ( $V_{3D} \sim 13.5$  km s $^{-1}$ ) then implies  $M_\star \gtrsim 7M_\odot$ . A second mass estimate can be derived by assuming that the material within the four arms is part of an outflowing wind (see § 4.3) and therefore must be moving at or near escape velocity. Taking the mean space velocities of the  $v=2$  masers within the four arms ( $V_{3D} \sim 16.0$  km s $^{-1}$ ) and a fiducial radius  $r \sim 25$  AU from Source I (roughly equal to the radius of the midpoint of the base of each arm from Source I) also implies a central mass of  $M_\star \gtrsim 7M_\odot$ . These kinematically-derived masses are somewhat smaller than the estimate of Reid et al. (2007) based on the 7-mm radio continuum luminosity ( $M_\star \approx 10M_\odot$ ). Since a star with  $M_\star \lesssim 7M_\odot$  would be unable to produce an H II region and would not have sufficient luminosity to power the SiO maser emission ( $L_\star \gtrsim 10^4 L_\odot$ ; Menten & Reid 1995), it therefore seems probable that Source I is somewhat higher than the above kinematically determined values—i.e.,  $M_\star \sim 8\text{--}10M_\odot$ .

If magnetic fields are threading the Source I disk and are responsible for powering the wind (see § 4.3.4), then the models described by Königl & Pudritz (2000) predict that only the material at the *base* of the wind is expected to exhibit Keplerian rotation. We therefore have measured the locations of the peak rotational velocity of the SiO emission along the northeastern edge of the dark band that runs parallel to the disk midplane (see Fig. 2). Taking a mean from the 19 epochs of data and from the red- and blue-shifted sides of the disk, we find  $|V_{\max}| \approx 19$  km s $^{-1}$  at  $r \approx 20$  AU. This implies  $M_\star \gtrsim 8M_\odot$ .

If dust is mixed with the SiO maser-emitting gas as proposed by Elitzur (1982), then radiation pressure on the grains could also influence the gas kinematics, assuming the grains can efficiently transfer some of their momentum to the gas. This would again lead to observed velocities that are smaller than predicted by Kepler’s Law for a given mass. However,

estimating the magnitude of this effect on the observed gas velocities will depend on the intrinsic stellar mass and luminosity, as well as the detailed properties of the grains—all of which are uncertain (e.g., Kwok 1975). Moreover, it is unclear whether dust could survive at the temperatures expected near the base of the Source I wind ( $T \gtrsim 2000$  K; Goddi et al. 2009a; see also below).

We emphasize that the interpretation of Source I as a single, luminous YSO with  $M_\star \sim 8\text{--}10M_\odot$  seems to provide the simplest explanation for *both* the radio continuum observations and the SiO maser kinematics. A binary of equivalent mass, or a less massive, less luminous star, would not be able to produce the observed radio continuum emission nor provide the necessary luminosity to power the SiO masers. On the other hand, a significantly more massive star would be difficult to reconcile with the observed SiO kinematics (i.e., the transverse motions in the bridges, which we interpret as material orbiting the central mass, and the systematically outward motions in the arms, which we interpret as material traveling at or near escape velocity). Our results therefore seem to be in contradiction with the scenario recently proposed by Gómez et al. (2008), in which Source I was ejected from a multiple stellar system  $\sim 500$  years ago and now comprises a tight binary with a mass in the range  $12 M_\odot < M_\star < 19 M_\odot$ .

In addition to the problem of the discrepancy between our derived mass for Source I and the value proposed by Gómez et al. (2008), accounting for the properties of Source I’s disk in such a picture (e.g., its size, density, and symmetry) might also be problematic. The passage of another star within  $\sim 230 \pm 70$  AU of Source I (see Gómez et al.) and the subsequent formation of a tight binary most likely would have disrupted any previously existing disk around Source I (e.g., Moeckel & Bally 2006), requiring formation of the existing disk structure within the past 500 yr. Nonetheless, under certain conditions, such rapid disk regrowth might be possible via either Bondi-Hoyle accretion or the tidal shredding of the interloper.

In the case of Bondi-Hoyle accretion, the Bondi radius of an accreting object of mass  $M$  is defined as  $r_B = GM/v_i^2$ , where  $G$  is the gravitational constant and  $v_i$  is a characteristic velocity, which may be taken to be the motion of the object with respect to the surrounding gas (e.g., Krumholz et al. 2006). From Goddi et al. (in prep.), the motion of Source I with respect to the ambient medium is  $v_i \sim 12$  km s $^{-1}$ , implying  $r_B \approx 50$  AU for  $M = 8M_\odot$ . Such a radius is comparable to the observed size of the Source I disk.

While the mass of the disk surrounding Source I is uncertain (see Reid et al. 2007), we can roughly estimate this quantity,  $M_d$ , by assuming the disk shape is a flattened cylinder with  $r \sim r_B = 50$  AU and  $h = 14$  AU (§ 3.1.1) and that the mean particle density is comparable to the value required to explain the SiO maser emission ( $n \approx 10^{10}$  cm $^{-3}$ ). Assuming the



bulk of the disk material is ionized, we adopt a mean molecular weight per particle of  $\mu=0.6$ , implying  $M_d \approx 0.002M_\odot$ . Given a time frame of 500 yr, this implies a minimum required mass flux  $\dot{M}_d \sim 4 \times 10^{-6} M_\odot \text{ yr}^{-1}$  (comparable to the mass *outflow* rate estimated from the SiO  $v=0$  emission; Greenhill et al., in prep.). Using Equation 1 of Krumholz et al. (2006), we can now estimate the required ambient density to support this mass accretion rate as  $\rho_a = \dot{M}_d v_i^3 [4\pi G^2 M_\star^2]^{-1} \approx 3.0 \times 10^{-17} \text{ g cm}^{-3}$ . Assuming the ambient material is purely molecular ( $\mu=2.3$ ) then implies an ambient particle density  $n_{\text{H}_2} \approx 8 \times 10^6$ . Although the latter value is rather high, it is comparable to values previously measured for the Orion hot core region (e.g., Masson & Mundy 1988 and references therein) and thus may be roughly consistent with plausible values for this Orion KL region. We conclude that in the absence of more sophisticated calculations, we cannot rule out disk augmentation or rebuilding via Bondi-Hoyle accretion may have occurred during the past 500 yr. However, we note that one additional caveat is that disks formed in this manner are predicted to have rather chaotic and asymmetric structures (e.g., Krumholz et al.), in contrast to the Source I case.

One additional scenario that might reconcile our new Source I measurements with the findings of Gómez et al. (2008) is the possibility that Source I has recently formed or altered its disk by tidally shredding a lower mass interloper (see Davies et al. 2006). If this interloper had a mass as high as  $M_\star \approx 3M_\odot$ , this would bring the total mass of the Source I system in marginal agreement with values proposed by Gómez et al. Furthermore, such an event might offer a natural explanation for the maser emission and outflows associated with Source I (see Bally & Zinnecker 2005). Nonetheless, this picture would likely require a considerably closer passage between the two stars than estimated by Gómez et al. (i.e., as close as a few tens of stellar radii; see Davies et al.). In addition, the relatively large resulting mass of the disk may in turn require an implausibly luminous central star in order to account for the observed radio continuum emission (see Reid et al. 2007).

In summary, while our latest observations of Source I present a compelling case for disk-mediated accretion in a massive YSO, it is clear that further modeling will be required to explore possible interaction scenarios and to better constrain whether such an event is likely to have influenced its present disk and outflow properties. New N-body simulations as well as further discussion of the interaction history of Source I will be presented by Goddi et al. (in preparation).

### 4.3. What Drives the SiO Maser Emission from Source I?

Because SiO maser emission is extremely rare around YSOs, its origin in the case of Source I has been another longstanding puzzle. Cunningham et al. (2005) proposed that the

Source I masers arise from a shear layer along the walls of a cavity that has been evacuated as a bipolar wind expands into a rotating, collapsing envelope. This model is able to reproduce the magnitudes and directions of the proper motions in the arms as well as the frothy appearance of the SiO-emitting material. However, the observed breadth of the arms appears to be greater than expected for an interface region. Moreover, this model cannot readily explain several other features of the SiO masers, including the transverse motions observed in the inter-arm bridges, the presence of groups of maser features beyond the four main arms (the “isolated” features in Fig. 2), or the linear trajectories of features that persist unperturbed over many months (Fig. 5, 9, & 10). The Cunningham et al. model also predicts higher densities along the outer edges of the arms (their Fig. 1), which appears to be inconsistent with our observation that the  $v=2$  masers (which preferentially occur in higher density gas) lie on average closer to Source I than the  $v=1$  masers (§ 3.1.1; Fig. 4).

Wright et al. (1995) proposed a slightly different scenario—namely that the SiO masers arise from material ablated from the surface of an accretion disk by a wind or outflow. Because our current observations provide evidence for the presence of an accretion disk, we now favor some variant of this “boiling disk” picture. Constraining the driving mechanism for this wind will require detailed modeling, but here we comment briefly on the likely applicability of various classes of disk wind models to the Source I case.

#### 4.3.1. *Disk Photoionization*

As discussed by Hollenbach et al. (1994), YSOs hot enough to produce an H II region are capable of mass-loss via photoevaporation of their disks as material is heated to temperatures in excess of the local escape temperature. In the “weak wind” case, an ionized flow is predicted to set in beyond the disk radius,  $r_g$ , where the sound speed is roughly equal to the escape speed. For Source I, if we take the sound speed as  $\sim 11$  km s<sup>-1</sup> (assuming  $T = 8000$  K on the surface of the ionized disk; Reid et al. 2007), a mean mass per particle of  $1.13 \times 10^{-24}$  g within the ionized disk (Hollenbach et al. 1994), and  $M_\star \approx 8M_\odot$ , this predicts  $r_g \approx 1 \times 10^{15}$  cm—roughly a factor of three larger than what is observed. In addition to this discrepancy, the outflowing material is predicted to be mostly ionized, raising the problem of how to maintain sufficient quantities of dense, molecular material in the disk wind and how to account for the SiO maser emission in the bridge regions.

#### 4.3.2. *Line-Driven Winds*

For hot stars, radiation pressure mediated by ultraviolet absorption line opacity offers another means of powering a wind. Classically, such winds tend to have velocities too high ( $\gtrsim 400 \text{ km s}^{-1}$ ) and densities too low ( $\rho \ll 10^{-14} \text{ g cm}^{-3}$ ) to readily account for the maser-emitting gas surrounding Source I (e.g., Lamers et al. 1995). Drew et al. (1998) showed that the presence of a rotating, circumstellar disk helps to produce a slower, denser wind along the equatorial direction. However, for  $M_\star \approx 10M_\odot$ , the characteristic wind speeds at more oblique angles (i.e., angles consistent with the outward motions along the arms of Source I) still are an order of magnitude too high to match those of the Source I SiO masers (see Drew et al.). Furthermore, the high poloidal velocities predicted by this model are inconsistent with outflow speeds inferred from other line tracers, such as SiO  $v=0$  emission (Goddi et al. 2009a; Greenhill et al., in preparation). It thus appears that line-mediated radiation pressure is unlikely to play a significant role in powering the outward migrations of the SiO maser-emitting gas around Source I.

#### 4.3.3. *Radiatively-Driven (Dust-Mediated) Winds*

Elitzur (1982) has suggested that gas and dust may be mixed within the zone from which the SiO maser emission arises around Source I. This would be in contrast to the situation in the extended atmospheres of evolved stars, where the SiO maser emission arises from a region just inside the dust-formation radius (e.g., Reid & Menten 1997). Elitzur further showed that in such a case, dust-mediated radiation pressure alone might be able to account for the outflow of material from Source I.

Although we cannot yet exclude this general class of model for driving the Source I wind, several of the previous assumptions made by Elitzur (1982) require revision as a result of more recent, high-resolution observations. For example, Elitzur assumed a luminosity for the Source I of  $10^5 L_\odot$ , which is likely an order of magnitude too high (Reid et al. 2007) and a mass-loss rate of  $10^{-3} M_\odot \text{ yr}^{-1}$ —two orders of magnitude larger than the value recently derived by Greenhill et al. (in preparation) based on SiO  $v=0$  measurements. Elitzur’s model also depends upon energy input by turbulent motions of  $\sim 7 \text{ km s}^{-1}$  in order to maintain the gas at a higher temperature than the dust (as otherwise the gas would rapidly thermalize to the dust blackbody temperature and population inversion could not be maintained). Such large turbulent motions are inconsistent with the low mean line-of-sight velocity dispersion of the maser-emitting material seen in our present data (Fig. 6) as well as with the ordered velocity field of the SiO masers (Fig. 7). Lastly, as already noted above, it would likely be difficult for grains to survive within  $\lesssim 100 \text{ AU}$  from Source I, particularly near the base of

the wind, where temperatures may be  $\gtrsim 2000$  K (Goddi et al. 2009a). Given these new developments, the dust-driven wind scenario for Source I now faces a number of challenges.

#### 4.3.4. *Magnetohydrodynamic Winds*

Apparent curved and helical trajectories of certain SiO maser features (§3.1.1 & 3.3), strongly hint that magnetic fields may play a role in shaping the dynamics of the Source I region. For example, it would seem difficult to explain features such as the streamer emanating from the Western bridge (Fig. 9) in the absence of magnetic fields. While pressure gradients within the disk might act to bend the paths of outflowing material, the observations of pronounced curvature at large vertical displacements from the plane would require that the pressure scale height of the disk is comparable to the observed vertical extent of the masers. Moreover, we see numerous proper motion trajectories that appear to be linear, including along the outer edges of the individual arms, contrary to what would be expected if pressure gradients were important. We therefore suggest that the streamers are more likely to be comprised of gas clumps constrained to move along a magnetic field lines like “beads on a wire” (see e.g., Blandford & Payne 1982).

Previous evidence for a magnetic field associated with Source I was provided by polarization measurements of the SiO  $v = 0$ ,  $J=1-0$  and  $J=2-1$  emission (Tsuboi et al. 1996; Plambeck et al. 2003). After correcting for Faraday rotation, the position angle for the polarization vectors derived by Plambeck et al. ( $57^\circ$ ) is consistent with magnetic field lines threading roughly perpendicular to the disk defined by the SiO masers and 7-mm continuum emission and parallel to the outflow direction traced by the SiO  $v = 0$  emission and the H<sub>2</sub>O masers (see Goddi et al. 2009a; Greenhill et al., in preparation).

Assuming a magnetic field is present, a magnetocentrifugal wind (e.g., Blandford & Payne 1982; Königl & Pudritz 2000) would be a natural candidate for powering a disk wind from Source I. In this scenario, gas clumps fragment from the disk, are swept outward along field lines by hydromagnetic forces (e.g., Emmering et al. 1992), and are induced to excite maser emission when irradiated, shocked, or heated by collisions. Magnetic phenomena may also provide an explanation for the elongated emission fronts visible in three of the arms. For example, tangled magnetic field lines (e.g., Kigure & Shibata 2005; Banerjee & Pudritz 2006) or instabilities within a magnetically-driven flow (e.g., Kim & Ostriker 2000) might account for the elevated velocity dispersions and rope-like morphologies of these features (see § 3.1.1). Doeleman et al. (1999) originally proposed that these elongated structures might arise at the shocked interfaces of an outflow. However, the observation that the emission fronts are not preferentially oriented perpendicular to the outflow direction (as expected for

shock fronts) seems to argue against this interpretation.

It is believed that a necessary condition for launching a magnetically-powered wind is that the vertical magnetic field is close to equipartition (e.g., Ferreira 2007)—i.e.,  $\frac{1}{2}nV^2 = \frac{1}{2}B^2\mu_0^{-1}$ , where  $n$  is the gas number density,  $V$  is the mean velocity of a gas molecule,  $B$  is the magnetic field strength, and  $\mu_0$  is the permeability of free space. Assuming  $n = 10^{10} \text{ cm}^{-3}$  (§ 3.1.1) and  $V=14.0 \text{ km s}^{-1}$  (§ 3.3), the implied magnetic field strength for Source I is  $\sim 0.3 \text{ G}$ . One possible source for this field might be the original interstellar magnetic field threading the molecular cloud out of which Source I was born. Based on measurements of OH 1665-MHz masers across a  $\sim 10^4 \text{ AU}$  region surrounding Source I, Cohen et al. (2006) derived field strengths of 1.8 to 16.3 mG. Since the OH masers are believed to arise from material with molecular hydrogen density  $n_{\text{H}_2} \sim 7 \times 10^6 \text{ cm}^{-3}$  (Gray et al. 1992), and magnetic field strength is expected to scale as the square root of the gas density, it is plausible that field strengths of order the value predicted by assuming equipartition might now be present within the denser, SiO-emitting gas.

Direct measurements of the magnetic field strength in the disk of Source I would be of considerable interest, both for understanding its role during the accretion/outflow process and for providing new clues on the nature of magnetic fields in B-type stars during later evolutionary stages. Little is presently known about the range of magnetic field strengths present in early-type B stars on the main sequence owing to the difficulty of measuring fields  $\lesssim 3 \text{ kG}$  in rapidly rotating stars (e.g., Landstreet 1992; Schnerr et al. 2008 and references therein). Moreover, it has been suggested that magnetic fields with strengths as low as a few Gauss and originating at the time of the star’s formation might account for the origin of magnetized neutron stars (Ferrario & Wickramasinghe 2005).

We note that even if magnetohydrodynamic forces are not the main driving mechanism for the Source I wind, magnetic forces may still play a key role in shaping the outflow, similar to what has been proposed for planetary nebulae (e.g., Blackman 2008 and references therein). In addition, magnetic fields may provide a mechanism to enhance the coupling between gas and dust grains, thereby increasing the efficiency of a possible dust-driven wind (Hartquist & Havnes 1992).

## 5. Summary

We have presented two multi-epoch movies chronicling the evolution of the  $^{28}\text{SiO } v=1$  and  $v=2, J=1-0$  maser emission surrounding Orion Source I over nearly two years. These movies comprise VLBA observations with  $\sim 0.5 \text{ mas}$  (0.2 AU) resolution and provide the most

detailed view ever obtained of the dynamics and temporal evolution of molecular material within  $\sim 20$ -100 AU of a massive YSO. We interpret the SiO masers surrounding Source I as arising from a wide-angle, bipolar wind that emanates from a rotating accretion disk viewed nearly edge-on. We find evidence to support the suggestion that magnetic fields are playing a role in shaping and/or powering this wind. The maser kinematics and proper motions, coupled with constraints from previous radio continuum observations, imply a mass for the central star of  $\gtrsim 8M_{\odot}$ . Our study provides compelling evidence that disk-mediated accretion and low-velocity, wide-angle winds are both key elements in the evolution of young stars in this mass range. However, we cannot exclude the possibility that a recent encounter has also played a role in shaping the properties of the Source I disk and outflow.

We thank Mark Reid for valuable technical discussions and for supplying his `fit_rates` code. We also acknowledge helpful discussions with Mark Krumholz and comments from our anonymous referee that have helped to improve our presentation. This project has been supported by NSF grant 0507478 and a Visiting Scientist appointment to LDM from the Smithsonian Astrophysical Observatory. The data presented here were part of NRAO programs BG118 and BG129.

## REFERENCES

- Alcolea, J., Bujarrabal, V., & Gallego, J. D. 1989, *A&A*, 211, 187
- Bally, J. & Zinnecker, H. 2005, *AJ*, 129, 2281
- Banerjee, R. & Pudritz, R. W. 2006, *ApJ*, 641, 949
- Blackman, E. G. 2008, in *Cosmic Magnetic Fields: From Planets to Stars and Galaxies*, IAU Symp. 259, ed. K. G. Strassmeier, A. G. Kosovichev, & J. E. Beckman, 35
- Blandford, R. D. & Payne, D. G. 1982, *MNRAS*, 199, 883
- Briggs, D. S. 1995, Ph.D. Dissertation, New Mexico Institute of Mining and Technology, Socorro, NM (<http://www.aoc.nrao.edu/ftp/dissertations/dbriggs/diss.html>), 64
- Bujarrabal, V. 1994a, *A&A*, 285, 953
- Bujarrabal, V. 1994b, *A&A*, 285, 971
- Bujarrabal, V., Castro-Carrizo, A., Alcolea, J., & Neri, R. 2005, *A&A*, 441, 1031
- Cohen, R. J., Gasipring, N., Meaburn, J., & Graham, M. F. 2006, *MNRAS*, 367, 541
- Cotton, W. D. 2007, *EVLA Memo* 116
- Cunningham, A., Frank, A., & Hartmann, L. 2005, *ApJ*, 631, 1010

- Davies, M. B., Bate, M. R., Bonnell, I. A., Bailey, V. C., & Tout, C. A. 2006, *MNRAS*, 370, 2038
- Desmurs, J. F., Bujarrabal, V., Colomer, F., & Alcolea, J. 2000, *A&A*, 360, 189
- Doeleman, S. S., Lonsdale, C. J., & Pelkey, S. 1999, *ApJ*, 510, L55
- Doeleman, S. S., Lonsdale, C. J., Kondratko, P. T., & Predmore, C. R. 2004, *ApJ*, 607, 361
- Elitzur, M. 1982, *ApJ*, 262, 189
- Emmering, R. T., Blandford, R. D., & Shlosman, I. 1992, *ApJ*, 385, 460
- Ferrario, L. & Wickramasinghe, D. T. 2005, *MNRAS*, 356, 615
- Ferreira, J. 2007, in *MHD Disc Winds*, *Lect. Notes Phys.*, 723, 181
- Goddi, C., Greenhill, L. J., Chandler, C. J., Humphreys, E. M. L., & Matthews, L. D. 2009a, *ApJ*, 698, 1165
- Goddi, C., Greenhill, L. J., Humphreys, E. M. L., Matthews, L. D., Tan, J. C., & Chandler, C. J. 2009b, *ApJ*, 691, 1254
- Gómez, L., Rodríguez, L. F., Loinard, L., Lizano, S., Allen, C., Poveda, A., & Menten, K. M. 2008, *ApJ*, 685, 333
- Gray, M. D., Field, D., & Doel, R. C. 1992, *A&A*, 262, 555
- Gray, M. D. & Humphreys, E. M. L. 2000, *New. Astron.*, 5, 155
- Greenhill, L. J., Gezari, D. Y., Danchi, W. C., Najita, J., Monnier, J. D., & Tuthill, P. G. 2004a, *ApJ*, 605, L57
- Greenhill, L. J., Gwinn, C. R., Schwartz, C., Moran, J. M., & Diamond, P. J. 1998, *Nature*, 396, 650
- Greenhill, L. J., Reid, M. J., Chandler, C. J., Diamond, P. J., & Elitzur, M. 2004b, in *Star Formation at High Angular Resolution*, *IAU Symp. 221*, *ASP Conf. Series*, ed. M. G. Burton, R. Jayawardhana, & T. L. Bourke, (ASP: San Francisco), 155
- Grève, J. P. 1980, *Ap&SS*, 72, 411
- Hartquist, T. W. & Havnes, O. 1994, *Ap&SS*, 218, 23
- Hasegawa, T., Morita, K.-I., Okurmura, S., Kaifu, N., Suzuki, H., Ohishi, M., Hayashi, M., & Ukita, N. 1986, in *Masers, Molecules, and Mass Outflows in Star Forming Regions*, ed. A. D. Haschick, (Haystack Observatory: Westford), 275
- Hollenbach, D., Johnstone, D., Lizano, S., & Shu, F. 1994, *ApJ*, 428, 654
- Kigure, H. & Shibata, K. 2005, *ApJ*, 634, 879
- Kim, W.-T. & Ostriker, E. C. 2000, *ApJ*, 540, 372

- Kim, M. Y. et al. 2008, PASJ, 60, 991
- Königl, A. & Pudritz, R. E. 2000, Protostars and Planets IV, ed. V. Mannings, A. P. Boss, and S. S. Russell, (Tucson: University of Arizona Press), 759
- Krumholz, M. R., McKee, C. F., & Klein, R. I. 2006, ApJ, 638, 369
- Kwok, S. 1975, ApJ, 198, 583
- Lamers, H. J. G. L. M., Snow, T. P., & Lindholm, D. M. 1995, ApJ, 455, 269
- Landstreet, J. D. 1992, A&AR, 4, 35
- Lockett, P. & Elitzur, M. 1992, ApJ, 399, 704
- Masson, C. R. & Mundy, L. G. 1988, ApJ, 324, 538
- Menten, K. M. & Reid, M. J. 1995, ApJ, 445, L157
- Menten, K. M., Reid, M. J., Forbrich, J., & Brunthaler, A. 2007, A&A, 474, 515
- Moeckel, N. & Bally, J. 2006, ApJ, 653, 437
- Piétu, V., Guilloteau, S., & Dutrey, A. 2005, A&A, 443, 945
- Plambeck, R. L., Wright, M. C. H., & Rao, R. 2003, ApJ, 594, 911
- Reid, M. J. & Menten, K. M. 1997, ApJ, 476, 327
- Reid, M. J., Menten, K. M., Greenhill, L. J., & Chandler, C. J. 2007, ApJ, 664, 950
- Schnerr, R. S. et al. 2008, A&A, 483, 857
- Shepherd, D. 2003, in Galactic Star Formation Across the Stellar Mass Spectrum, ASP Conf. Series, Vol. 287, ed. J. M. De Buizer and N. S. van der Blik, 333
- Soria-Ruiz, R., Alcolea, J., Colomer, F., Bujarrabal, V., Desmurs, J.-F., Marvel, K. B., & Diamond, P. J. 2004, A&A, 426, 131
- Tan, J. 2008, in Massive Star Formation: Observations Confront Theory, ASP Conf. Series, Vol. 387, ed. H. Beuther, H. Linz, & T. Henning, (ASP: San Francisco), 346
- Tsuboi, M., Ohta, E., Kasuga, T., Murata, Y., & Handa, T. 1996, ApJ, 461, L107
- Wright, M. C. H., Plambeck, R. L., Mundy, L. G., & Looney, L. W. 1995, ApJ, 455, L185
- Yi, J., Booth, R. S., Conway, J. E., & Diamond, P. J. 2005, A&A, 432, 531
- Zapata, L. A., Menten, K., Reid, M., & Beuther, H. 2009, ApJ, 691, 332
- Zinnecker, H. & Yorke, H. W. 2007, ARA&A, 45, 481



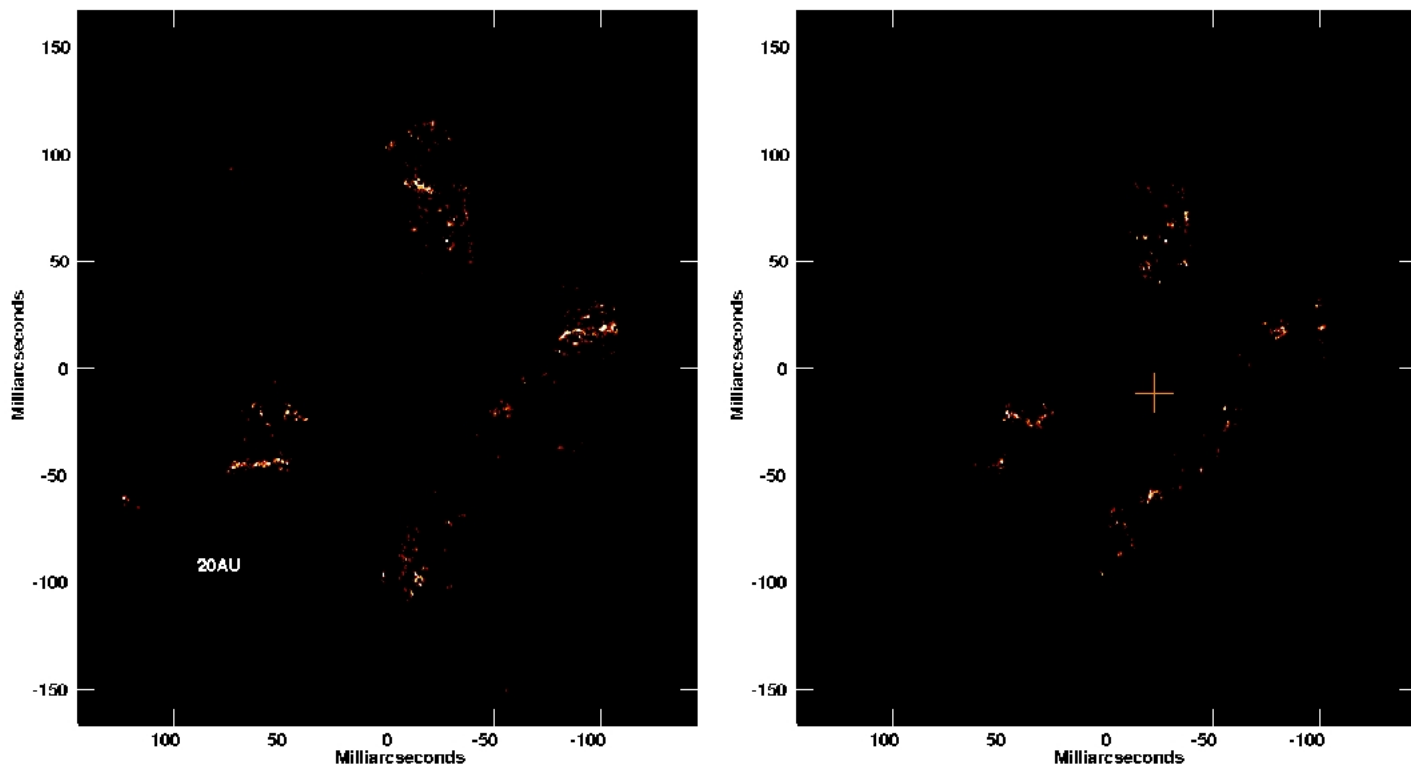


Fig. 1.— Velocity-integrated total intensity images of the  $^{28}\text{SiO } v=1, J=1-0$  emission (left) and the  $v=2, J=1-0$  emission (right) surrounding Source I as observed with the VLBA on 2001 March 19. An intensity range of 150 to 5000  $\text{Jy beam}^{-1} \text{ m s}^{-1}$  is shown using a logarithmic transfer function. The cross in the right panel indicates the calculated position of the Source I radio continuum source based on the fringe rate analysis from BG129E (Table 2) and the absolute position and proper motion measurements of Goddi et al. (in preparation). Note that this position is slightly displaced from the origin (0,0).

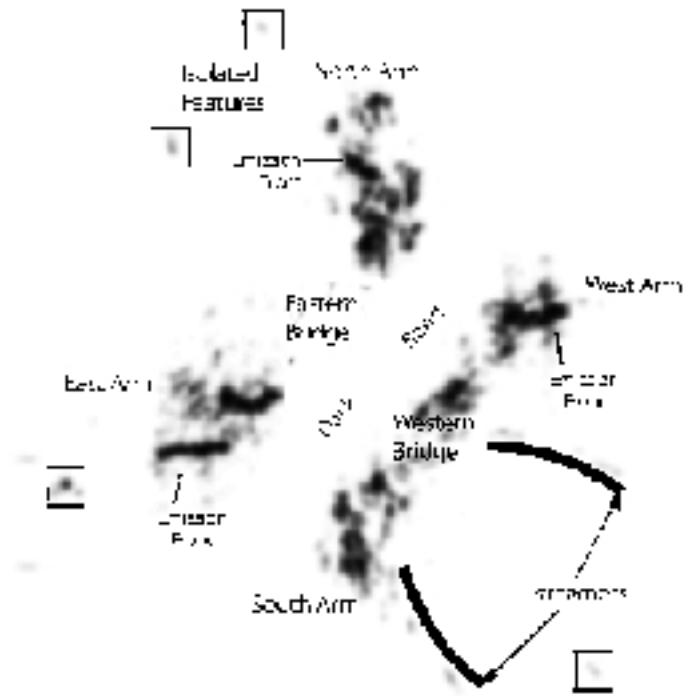


Fig. 2.— Schematic cartoon illustrating several key features of the Source I maser distribution that are discussed in the Text.

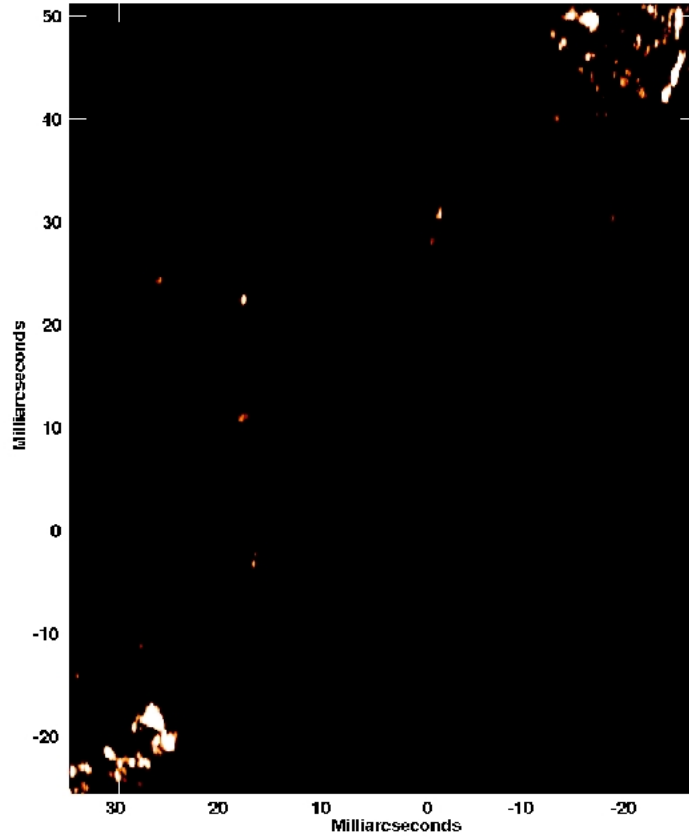


Fig. 3.— Total intensity map showing the combined  $^{28}\text{SiO}$   $v=1$  and  $v=2$ ,  $J=1-0$  emission within the Eastern bridge region (cf. Fig. 2) on 2002 June 28. Part of the base of the North arm is visible in the upper left corner, and the top of the East arm is visible in the lower left. The intensity range shown is 0 to  $500 \text{ Jy beam}^{-1} \text{ m s}^{-1}$  using a logarithmic transfer function.

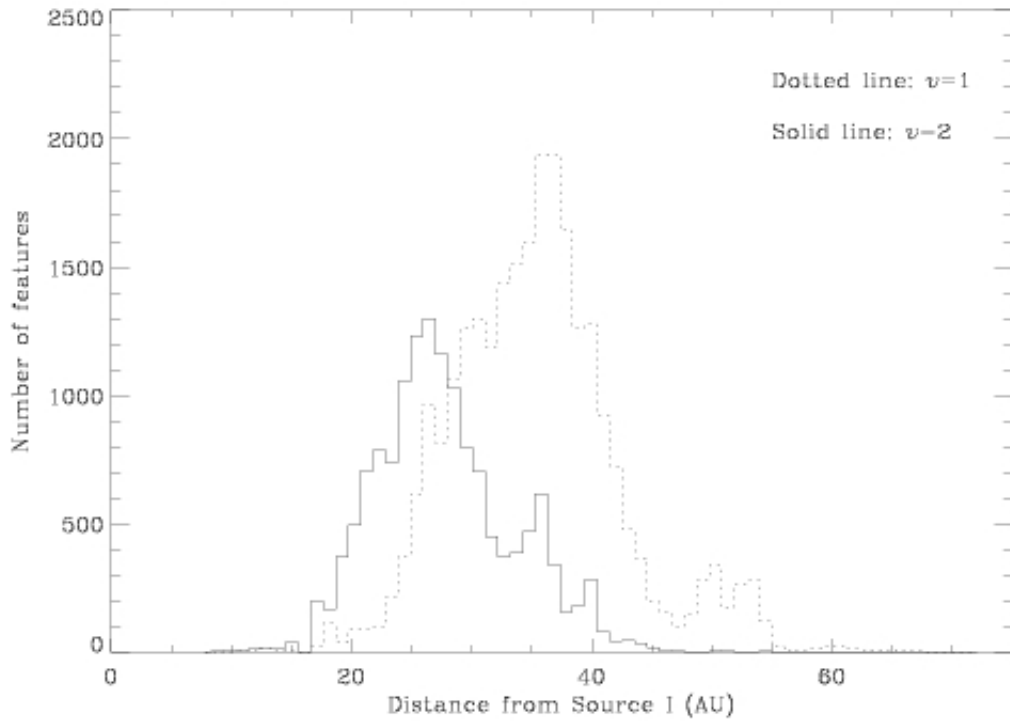


Fig. 4.— Histograms showing the total number of discrete maser features observed in the  $^{28}\text{SiO}$   $v=1$  transition (dotted line) and the  $v=2$  transition (solid line) over the course of 19 epochs. Discrete features were identified using an automated algorithm as described in § 3.3. Only features arising within the four main arm regions (cf. Fig. 2) are plotted. Bin sizes are 1.0 AU. Positions were measured relative to the position of Source I as indicated on Fig. 1a.

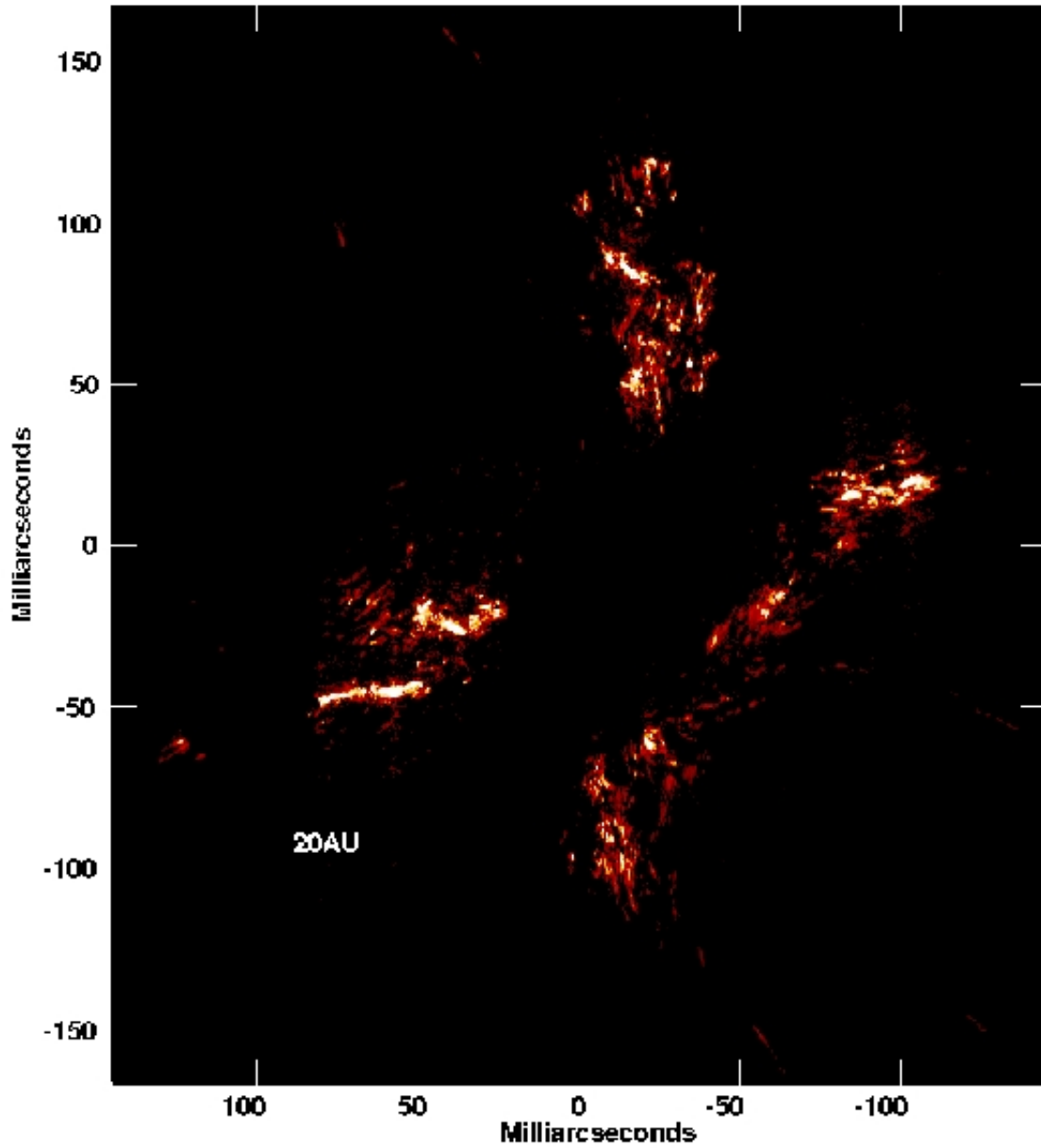


Fig. 5.— Total intensity map showing the combined  $^{28}\text{SiO}$   $v=1$  and  $v=2$ ,  $J=1-0$  emission distribution, summed over 19 observing epochs (see Table 1). An intensity range of 25 to 30000  $\text{Jy beam}^{-1} \text{ m s}^{-1}$  is shown using a logarithmic transfer function. A GIF animation showing the individual frames comprising this figure is available at <http://www.cfa.harvard.edu/kalypso/Figure5b.gif>.

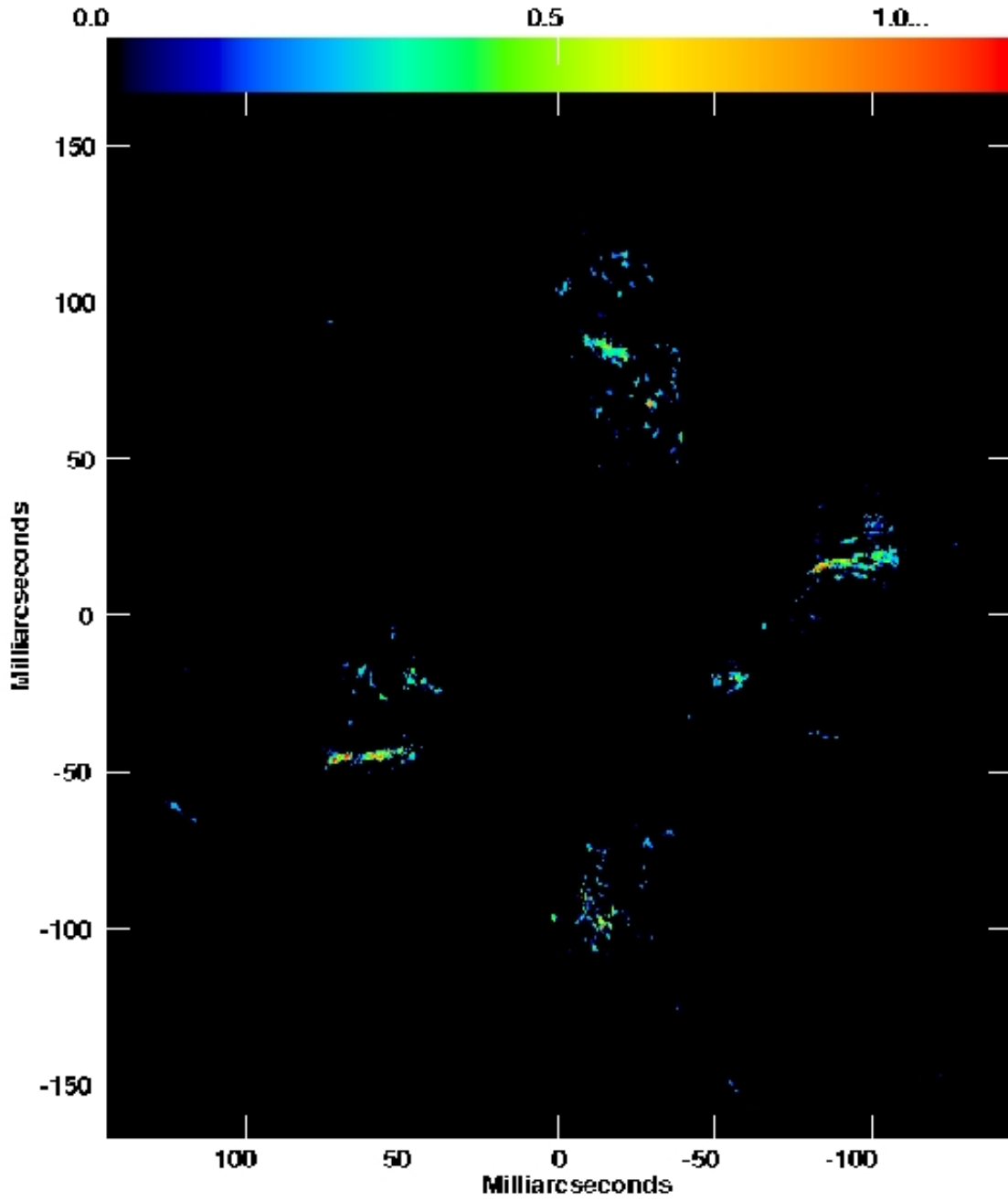


Fig. 6.— Map of the line-of-sight velocity dispersion (in  $\text{km s}^{-1}$ ) for the SiO  $v=1$  transition on 2001 May 18. The color bar is labeled in units of  $\text{km s}^{-1}$ . The peak dispersion for this epoch is  $\sim 3 \text{ km s}^{-1}$ .

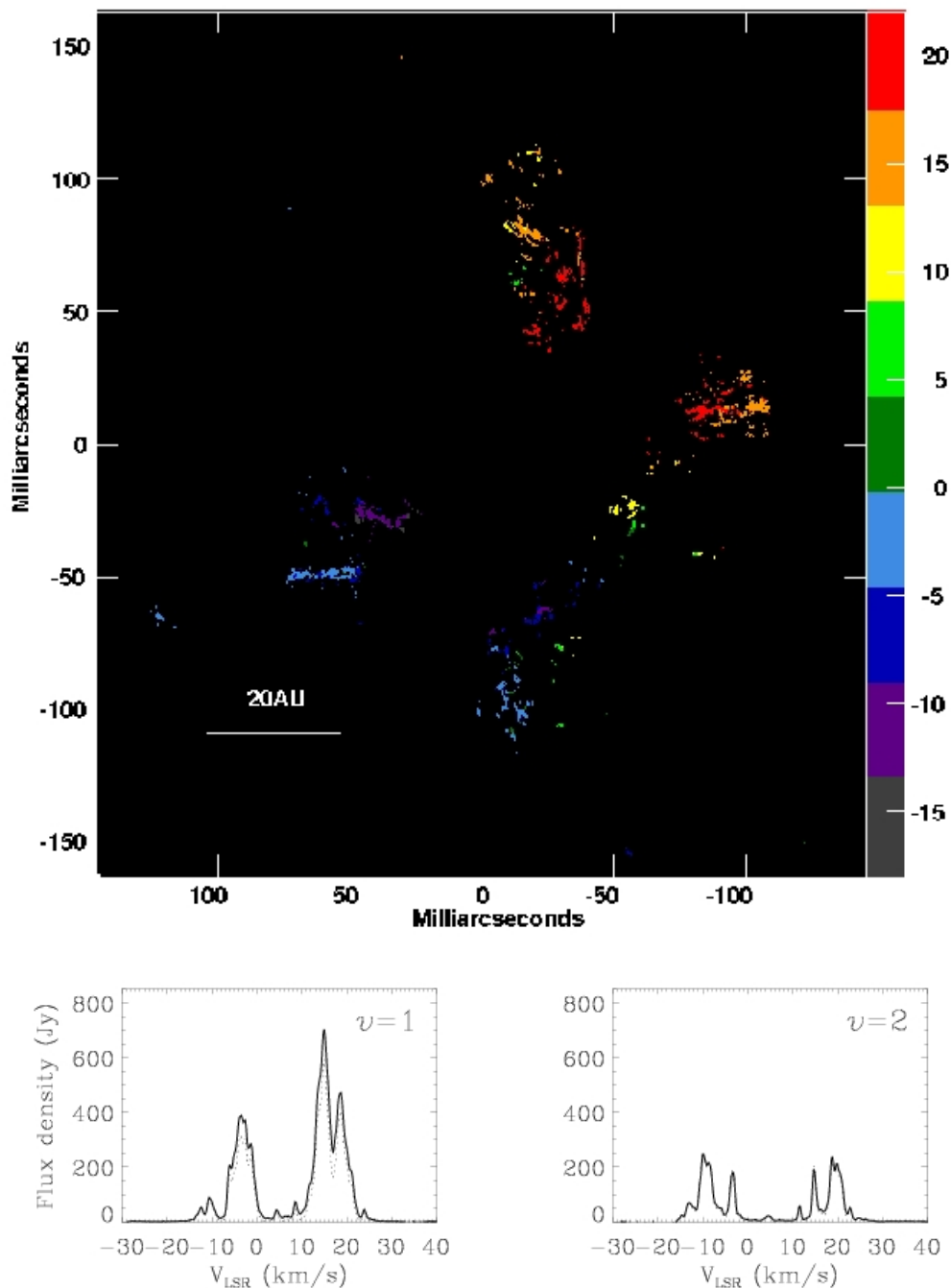


Fig. 7.— Velocity field of the  $^{28}\text{SiO}$   $v=1$  and  $v=2$ ,  $J=1-0$  emission surrounding Orion Source I as observed on 2001 March 19. The colors indicate measured radial velocities in  $\text{km s}^{-1}$ . Corresponding integrated spectra are also shown; in these panels the solid lines show total power spectra and the dashed lines show spectra derived from the imaged data. Axes of the spectra are LSR velocity in  $\text{km s}^{-1}$  and flux density in Jy. The full velocity spread of the emission varied from epoch to epoch, but was typically  $\sim 40 \text{ km s}^{-1}$  in  $v=1$  and  $\sim 42 \text{ km s}^{-1}$  in  $v=2$ . A GIF animation of this figure is available at <http://www.cfa.harvard.edu/kalypso/Figure7c.gif>.

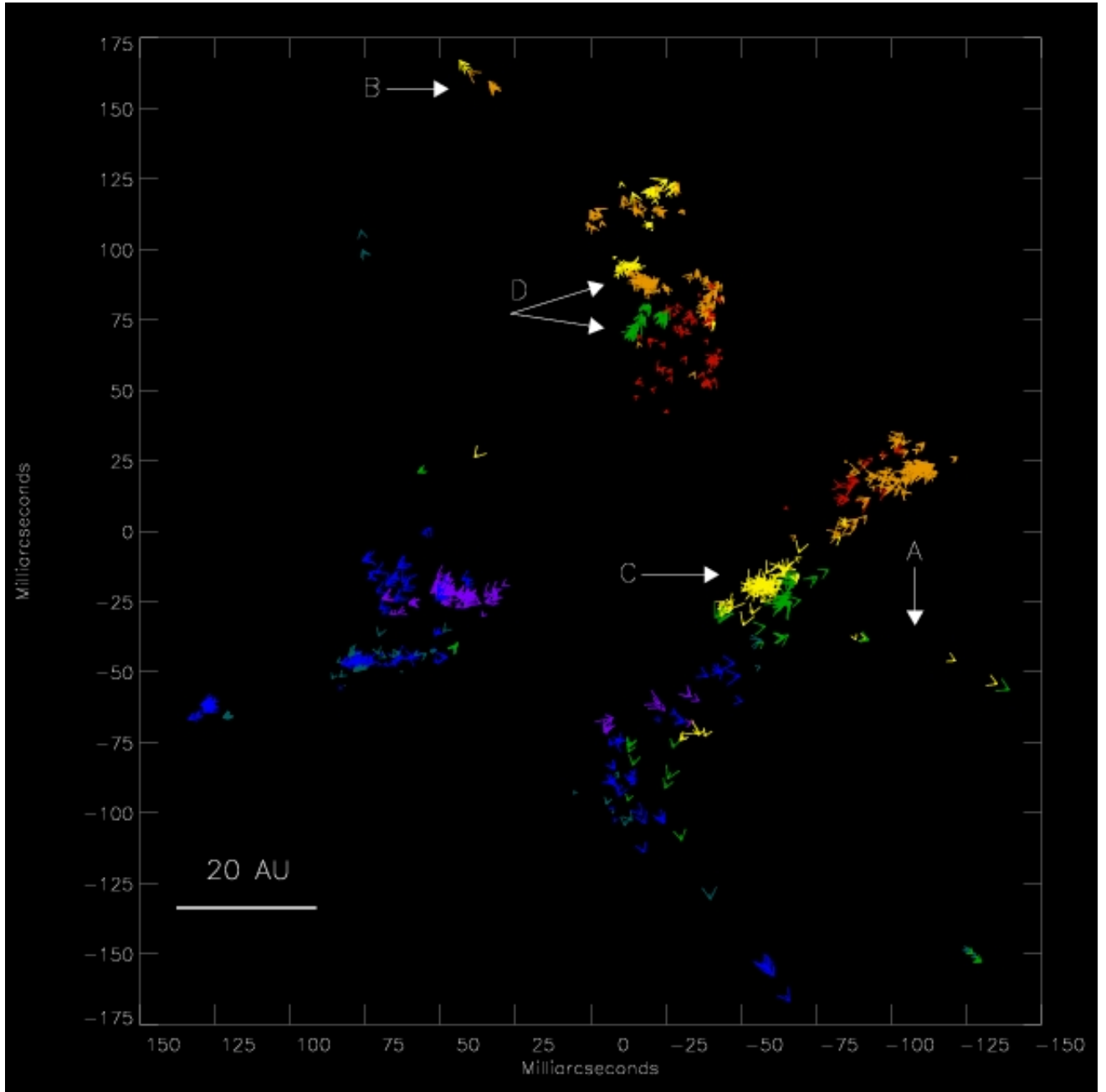


Fig. 8.— Proper motions of individual SiO maser features over the course of 21 months. Both  $v=1$  and  $v=2$  measurements are shown. The *color* of each arrowhead corresponds to its radial velocity (see Fig. 7 color bar); the *size* of each arrowhead is proportional to the transverse velocity (values range from  $0.8 \text{ km s}^{-1}$  to  $24.0 \text{ km s}^{-1}$ ); the *length* of each arrow stem indicates the distance transversed in the plane of the sky over three months (bridge regions) or four months (all other regions). Some key features described in the Text (§ 3.3) are designated by white letters and arrows.



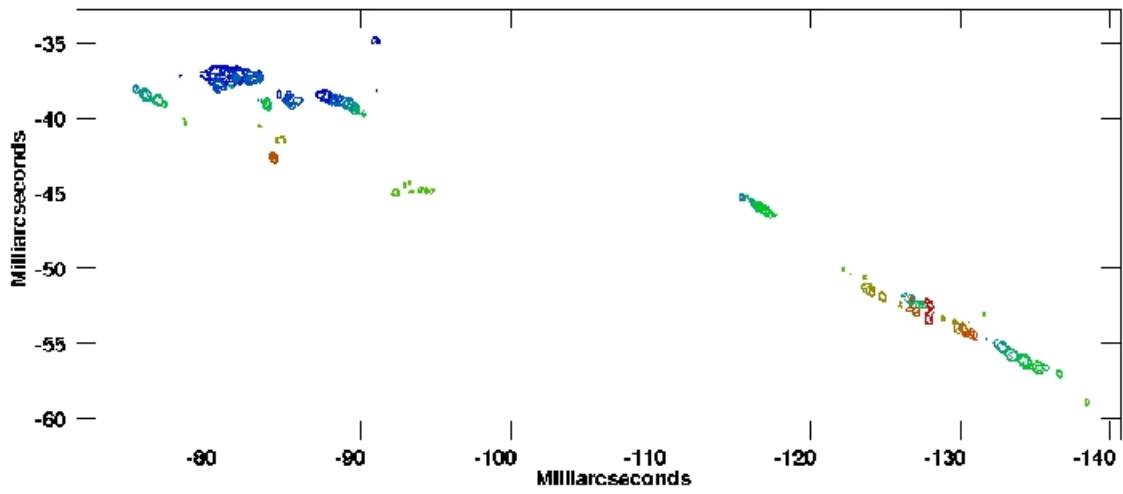


Fig. 9.— SiO  $v=1$  total intensity contours of a “streamer” (see Fig. 2 and Fig. 8, feature “A”). Data from 17 epochs are superposed, with each epoch contoured in a different color. Earlier epochs are shown in blue tones and later epochs in red tones. Contour levels are  $(4,8,\dots,2048)\times 10 \text{ Jy m s}^{-1}$ .

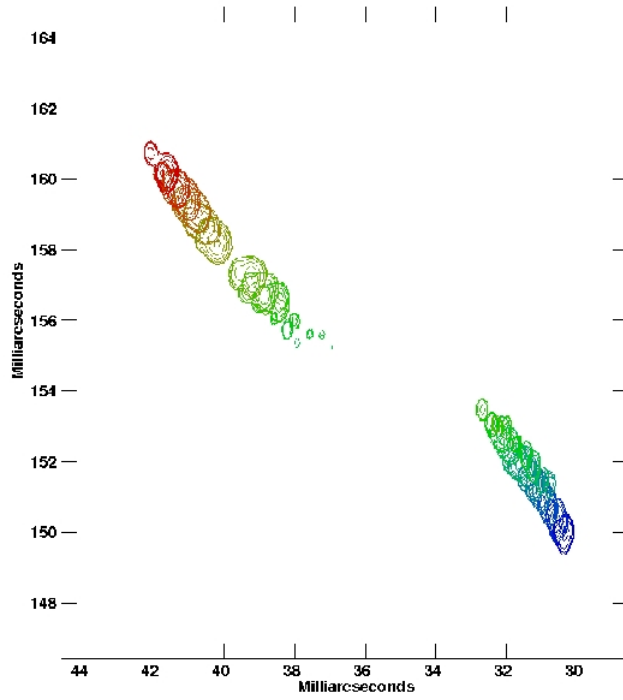


Fig. 10.— Similar to Fig. 9, but for one of the “isolated features” to the north of Source I (see Fig. 2 and Fig. 8, feature “B”). Data from 19 epochs are shown. The gap in the upper feature corresponds to a two-month period where no data were obtained (see Table 1). Contour levels are  $(4,8,\dots,2048)\times 10 \text{ Jy m s}^{-1}$ .